

# Development of Citrate-Based Dual-Imaging Enabled Biodegradable Electroactive Polymers

Dingying Shan, Sri-Rajasekhar Kothapalli, Dino J. Ravnice, Ethan Gerhard, Jimin P. Kim, Jinshan Guo, Chuying Ma, Jiazhi Guo, Li Gui, Lin Sun, Di Lu,\* and Jian Yang\*

Increasing occurrences of degenerative diseases, defective tissues, and severe cancers heighten the importance of advanced biomedical treatments, which in turn enhance the need for improved biomaterials with versatile theranostic functionalities yet using minimal design complexity. Leveraging the advantages of citrate chemistry, a multifunctional citrate-based biomaterial platform is developed with both imaging and therapeutic capabilities utilizing a facile and efficient one-pot synthesis. The resulting aniline tetramer doped biodegradable photoluminescent polymers (BPLPATs) not only possess programmable degradation profiles (<1 to > 6 months) and mechanical strengths ( $\approx 20$  MPa to >400 MPa), but also present a combination of intrinsic fluorescence, photoacoustic (PA), and electrical conductivity properties. BPLPAT nanoparticles are able to label cells for fluorescence imaging and perform deep tissue detection with PA imaging. Coupled with significant photothermal performance, BPLPAT nanoparticles demonstrate great potential for thermal treatment and *in vivo* real-time detection of cancers. The results on BPLPAT scaffolds demonstrate 3D high-spatial-resolution deep tissue PA imaging (23 mm), as well as promote growth and differentiation of PC-12 nerve cells. It is envisioned that the biodegradable dual-imaging-enabled electroactive citrate-based biomaterial platform will expand the currently available theranostic material systems and open new avenues for diversified biomedical and biological applications via the demonstrated multifunctionality.

## 1. Introduction

The past decades have witnessed the rise of biomaterials as an effective tool to redress the insufficiency of traditional drug and surgery based treatments for degenerative diseases, defects, and cancers,<sup>[1–3]</sup> as biomaterials have become pervasive in surgery, tissue engineering, drug delivery, and medical devices. However, to provide more effective and targeted therapies, there exists a need for novel biomaterials with versatile functionalities (degradability, biocompatibility, mechanical properties, etc.) to fulfill the comprehensive mechano-electro-chemical-biological requirements *in vivo*.<sup>[4,5]</sup> While multifunctionality can be achieved by combining materials and additives, such strategies often lead to prohibitive processing complexity and undesired safety concerns, limiting clinical translation.<sup>[6]</sup> To balance the need for safety, functionality, and simplicity, a biomaterial platform with a high degree of designability of chemical, biological, and structural features utilizing efficient synthesis and processing methods is greatly desired.

D. Shan, E. Gerhard, J. P. Kim, Dr. J. Guo, C. Ma, Prof. J. Yang  
Department of Biomedical Engineering  
Materials Research Institute  
The Huck Institutes of The Life Sciences  
The Pennsylvania State University  
University Park  
PA 16802, USA  
E-mail: jxy30@psu.edu

Prof. S.-R. Kothapalli  
Department of Biomedical Engineering  
The Pennsylvania State University  
University Park  
PA 16802, USA

Prof. S.-R. Kothapalli  
Penn State Hershey Cancer Institute  
Hershey, PA 17033, USA

DOI: 10.1002/adfm.201801787

Prof. D. J. Ravnice  
Department of Surgery  
Penn State Hershey Medical Center  
Hershey, PA 17033, USA

Prof. J. Guo, Prof. D. Lu  
Biomedical Engineering Research Center  
Kunming Medical University  
Kunming 650500, China  
E-mail: ludi20040609@126.com

Prof. L. Gui  
Department of Endocrinology  
The Third People's Hospital of Yunnan Province  
Kunming 650011, China

Prof. L. Sun  
Department of Cardiology  
The Second Affiliated Hospital  
Kunming Medical University  
Kunming 650101, China

To address this challenge, researchers have developed a new class of biocompatible and biodegradable citrate-based polyester elastomers by leveraging the reactive nature of citric acid in a cost effective, catalyst free, one pot polycondensation reaction of citric acid and diol monomers.<sup>[7,8]</sup> The presence of four functional groups per citrate molecule facilitates modification with additional moieties through pendant groups, as well as the generation of cross-linked networks. Citric acid is thus capable of acting as a keystone molecule, leading to a family of citrate-based materials with inherent physical, chemical, and/or biological functionalities, including tunable degradation rates and mechanical strengths, tissue adhesion, antimicrobial, antioxidant, and fluorescence.<sup>[9–16]</sup> Concurrently, ease of fabrication has allowed widespread applications of citrate-based biomaterials including tissue engineering (bone, skin, blood vessel, etc.),<sup>[12,17,18]</sup> drug delivery,<sup>[19]</sup> bioimaging,<sup>[14,16]</sup> and biosensing.<sup>[20,21]</sup>

Among these functionalities, bioimaging is a vital component in theranostic systems, as biomaterials that enable in situ imaging can assess material degradation, track drug delivery, and identify particular diseased tissues to treat cancers and degenerative diseases.<sup>[22–24]</sup> In particular, fluorescence-based imaging modalities provide high temporal resolution and sensitivity, real-time imaging, cost effectiveness, and use of maneuverable instruments.<sup>[24–26]</sup> We have recently developed a novel family of biodegradable photoluminescent citrate-based polymers (BPLPs),<sup>[14]</sup> in which the reaction of citric acid and an amino acid forms an intrinsic fluorescent moiety that has been used to track scaffolds and nanoparticles in vivo.<sup>[16]</sup> The resulting BPLPs demonstrated strong fluorescence properties including high quantum yield, tunable emission, and photostability, as well as biodegradability and biocompatibility, providing significant advantages over traditional fluorescent materials that conjugate or encapsulate organic dyes and cytotoxic quantum dots. Despite these benefits, fluorescence imaging in vivo with BPLPs is limited by low spatial resolution and imaging depths of only a few millimeters.

To overcome the limitations of single modality imaging technologies, multimodal imaging has drawn extensive attention due to its ability to provide more comprehensive spatial, temporal, structural, and high-resolution information.<sup>[27–29]</sup> Photoacoustic (PA) imaging, for example, may significantly complement fluorescence imaging systems by providing additional contrast, depth penetration, and 3D imaging capability.<sup>[30–32]</sup> Therefore, in this work, we sought to incorporate conductive aniline tetramer (AT) moieties into BPLPs to create a new family of dual imaging (fluorescence and PA) BPLP-AT elastomers, since conductive polymers such as polyaniline (PANI)<sup>[33]</sup> and polypyrrole<sup>[34]</sup> have been well demonstrated as PA contrast agents with strong near-infrared (NIR) absorption. In addition to dual-modality imaging, the integration of conductive moieties into our BPLP platform imparted significant electroactivity and photothermal properties of the resulting BPLP-AT elastomers, enhancing therapeutic potential through the transfer of chemical, physical, and electrical signals in biological systems to effectively modulate cellular activities.<sup>[35–38]</sup> Indeed, BPLP-ATs herein demonstrated improved cellular growth and differentiation in PC-12 cells, particularly in response to electrical stimulus, providing significant advantages over traditional

conductive polymers that suffer from poor solubility and processability, brittle mechanics, and nondegradability.<sup>[39–41]</sup>

In contrast to the complex, multicomponent design of traditional theranostic systems, we herein introduce a new family of biodegradable citrate-based elastomers that integrates dual-modality diagnostic imaging with electroactive and photothermal therapeutics via a convenient, one-pot polycondensation reaction, enabling a seamless platform with theranostic potential for disease prediagnosis, treatment, and postsurgical monitoring.

## 2. Results and Discussion

### 2.1. Synthesis of BPLPAT Pre-polymers

An irreversible decrease in electrical conductivity occurs when PANI is subjected to temperature above 100 °C, and in addition, the conductivity becomes unstable at temperatures above 150 °C.<sup>[42,43]</sup> In order to keep the balance between the conductivity of AT and reaction effectiveness, BPLPAT pre-polymers were synthesized by the polycondensation reaction of citric acid (CA), 1,8-octanediol (OD), L-cysteine, and AT at 110 °C (Figure S1, Supporting Information). With abundant reactive side carboxyl and hydroxyl groups, BPLPAT pre-polymers can be further reacted to form cross-linked polymeric networks (Figure 1a,b), and are expected to present fluorescence and PA properties to enable dual-modality imaging, as well as significant electroactivity to modulate cellular growth and differentiation (Figure 1c). In order to achieve the applicable functionalities of designed BPLPATs, we first verified the structures of the resulting BPLPAT pre-polymers with attenuated total reflectance-Fourier transform infrared (ATR-FTIR) and proton nuclear magnetic resonance (<sup>1</sup>H-NMR). In ATR-FTIR (Figure 1d), the absorption peak at 1705 cm<sup>-1</sup> represents the ester group (–C(=O)OR), the broad peak at 2936 cm<sup>-1</sup> (–CH<sub>2</sub>–) of the methylene group is from OD, and the absorption peak at 3372 cm<sup>-1</sup> comes from hydroxyl groups (–OH). The two peaks at 1488 and 1568 cm<sup>-1</sup> in the spectra of BPLPATs are attributed to the vibration of the quinoid ring and benzene ring from AT. We measured the areas under the absorption peaks of 1488 cm<sup>-1</sup> (quinoid ring from AT) and 1705 cm<sup>-1</sup> (–C(=O)OR) in ATR-FTIR spectra, and calculated their ratios. The result herein suggests that the proportion of AT in BPLPAT pre-polymers gradually increases from BPLP to BPLPAT15%. In <sup>1</sup>H-NMR spectra of BPLPATs (Figure 1e), peaks at 1.25 and 1.52 ppm represent –CH<sub>2</sub>– from OD, and the multiple peaks at 2.75 ppm represent –CH<sub>2</sub>– from CA. Two peaks at 5.60 (b) and 7.15 (a) ppm are assigned to the fluorophore formed by a condensation reaction between CA and L-cysteine. Protons (c-t) from AT are represented by multiple peaks between 6.38 and 7.78 ppm. During the synthesis process, OD and AT compete with each other to react with carboxyl groups from CA. By calculating integrals of peaks coming from protons (c-t) from AT and peaks representing –CH<sub>2</sub>– from OD, ratios of AT to OD in pre-polymers were obtained, indicating increased AT content in the obtained pre-polymers from BPLP to BPLPAT15%. Both ATR-FTIR and <sup>1</sup>H-NMR results confirmed the successful synthesis of BPLPAT pre-polymers with component ratios as designed.

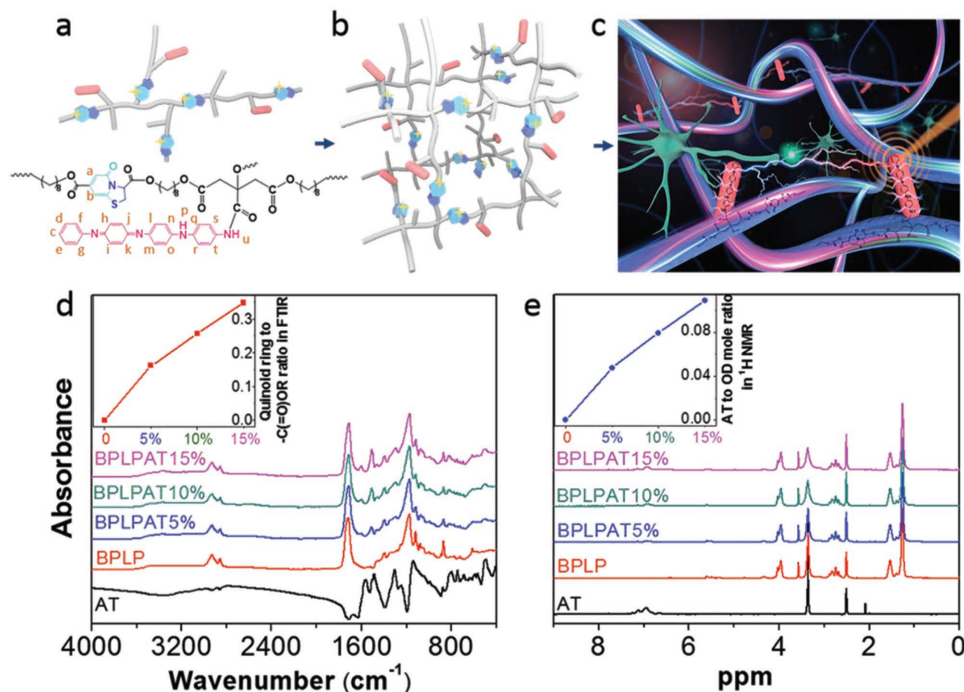


**Figure 1.** Characterization of BPLPAT polymer structure. a) Schematic and chemical structure of BPLPAT pre-polymers. b) Schematic of cross-linked BPLPAT structure. c) Schematic of functionalities (fluorescence imaging, PA imaging, and conductivity that promote cell communications) of cross-linked BPLPATs. d) ATR-FTIR spectra of AT, BPLP, and BPLPAT pre-polymers. Inset: quinoid ring to  $-C(=O)OR$  ratios increase with the increasing concentration of AT in polymer syntheses. e)  $^1H$  NMR spectrum of AT, BPLP, and BPLPAT pre-polymers. Inset: AT to OD molar ratios increase with the increasing concentration of AT in polymer syntheses.

## 2.2. Electrochemical Properties and Conductivities of BPLPAT Materials

As electroactivity determines the main biological functionalities of BPLPATs, we performed a systematic study of the electrochemical and conductive properties of BPLPATs using Autolab PGSTAT-302N and UV-2450 spectrometer. In the obtained cyclic voltammogram (CV) curves (Figure 2a), all BPLPAT groups (BPLPAT5%, BPLPAT10%, and BPLPAT15%) present characteristic oxidation and reduction transition peaks of AT. The CV curves of BPLPATs exhibit two oxidation/reduction peaks around 0.38 and 0.69 V, which correspond to AT's structure transition from the leucoemeraldine base state to the emeraldine state, and from the emeraldine state to the pernigraniline state. The UV absorption spectra of AT and BPLPAT10% presented two peaks at around 320 and 590 nm, which are assigned to the  $\pi-\pi^*$  transition of the benzenoid ring and the excitonic transition from the benzenoid ring to the quinoid ring, respectively. After doping AT and BPLPAT10% solutions with camphorsulfonic acid (CSA), two new absorption peaks at about 430 and 800 nm together with a slight blue shift of the benzenoid absorption peak to 308 nm appeared in their spectra due to the formation of delocalized polarons, which indicate the generation of a conductive phase of emeraldine salts (Figure 2b). The results from both CV curves and UV spectra confirmed the favorable electrochemical properties of BPLPATs. The conductivities of the BPLPAT films doped with CSA were increased from  $1.06 \times 10^{-7}$  to  $2.94 \times 10^{-6}$  S  $cm^{-1}$  with increasing AT content (Table S1, Supporting Information),

which fall within an order of conductivities that may sufficiently support the signal transduction and chemical exchange between cells *in vivo*.<sup>[41]</sup> Thus, the introduction of AT can impart favorable and tunable electrochemical and conductive properties to BPLPAT materials, which makes BPLPATs promising in regulating biological activities such as migration, proliferation, differentiation, and stimulating tissue regeneration.

## 2.3. In Vitro Degradation Properties of BPLPAT Materials

As the favorable degradation of BPLPs has been previously demonstrated, we next sought to assess how the introduction of AT into BPLP impacts on the degradation of the resultant polymers. Representatively, *in vitro* degradation studies were conducted on BPLP and BPLPAT10% pre-polymers (Figure 2c), as well as their cross-linked films (Figure 2d). Before cross-linking, BPLP and BPLPAT10% pre-polymers displayed similar degradation rates. After cross-linking, BPLPAT10% films degraded much slower than BPLP films. BPLP films completely degraded within 18 weeks, whereas BPLPAT10% films still had more than 20% mass remaining after 24 weeks. As indicated from the degradation studies, BPLPAT materials presented degradability with fine adjustment of degradation rates ranging from about three weeks to over six months within the formulations investigated. It is well-known that material degradation is a key design parameter of a material when used in biomedical applications such as tissue engineering and drug delivery. Material degradation rate significantly affects cell viability, cell

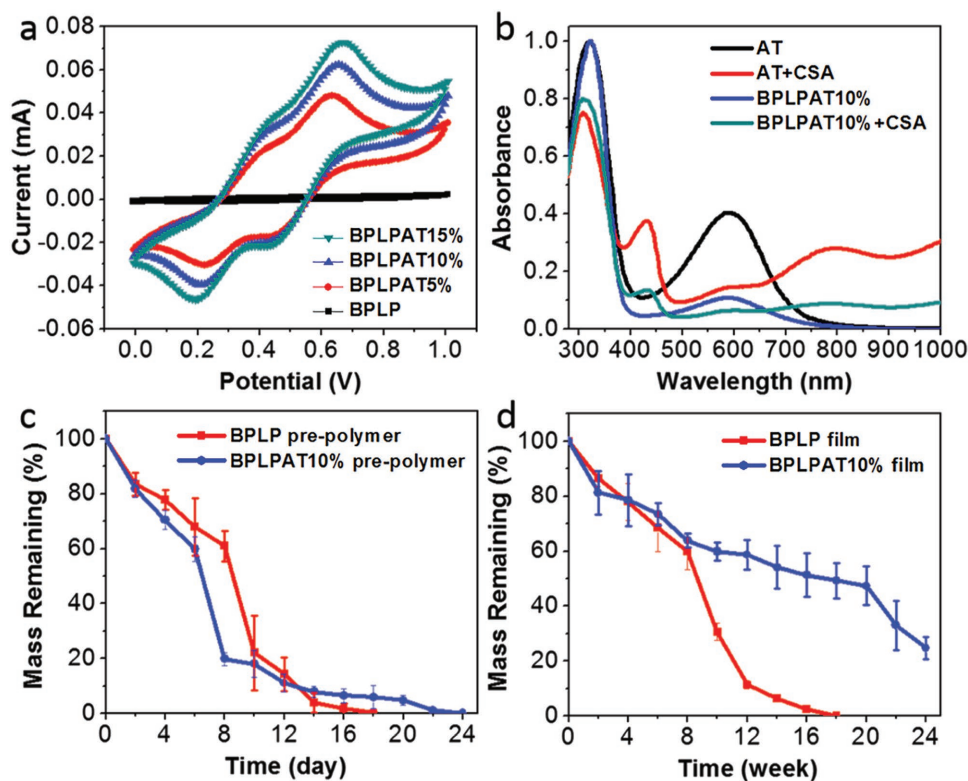


**Figure 2.** Electrochemical properties and in vitro degradation properties of BLPATs. a) The cyclic voltammogram (CV) curves of BPLP and BLPATs doped with CSA. b) The UV spectra of AT, CSA doped AT, BPLPAT10%, and CSA doped BPLPAT10%. c) In vitro degradation of BPLP and BPLPAT10% pre-polymers. d) In vitro degradation of BPLP and BPLPAT10% films.

migration, tissue infiltration and remodeling, angiogenesis, and life-span of medical devices.<sup>[44]</sup> With the tunable degradability, BLPATs may be designed with optimum degradation rates to meet specific application requirements.

#### 2.4. Mechanical Properties of BLPAT Films and Scaffolds

As material stiffness is known to significantly influence cellular activity, biomaterials with tissue-specific mechanical properties are essential for in vivo applications. We thus performed tensile mechanical tests of our BLPAT materials (Figure 3). For dry BLPAT polymer films, initial modulus increased about 80 times from BPLP ( $5.21 \pm 1.15$  MPa) to BPLPAT15% ( $409.24 \pm 7.75$  MPa) (Figure 3a). The increased AT content also led to increased tensile stress (Figure 3b) accompanied by decreased tensile strain, except for BPLPAT5%, which has comparable strain to BPLP (Figure 3c). The mechanical properties of BLPAT films were significantly regulated by the addition of AT, also evidenced by the shape of the tensile stress–strain curves (Figure 3g). BPLP, BPLP5%, and BPLPAT10% films all presented classical stress–strain curves of elastomers, while BPLPAT15% presented a curve characteristic of plastic deformation. As wet conditions are important considerations in biological applications, we also investigated the tensile properties of wet films (Figure 3h). After soaking in phosphate-buffered saline (PBS, pH=7.4) for 24 h, all BLPAT groups exhibited flexible elastic properties. The introduction of AT into BPLP not only increased the initial

modulus and the tensile stress of BLPATs (Figure 3d,e), but also increased their elongation (Figure 3f), which was attributed to the enhanced hydrogen bonding between BLPAT polymers. In addition, mechanical properties of BLPAT scaffolds in compression were also tested. The results indicated that the initial modulus and peak stress of BLPAT scaffolds in compression were also regulated by the addition of AT (Figure 3i,j).

One significant drawback of BLPs is their poor mechanical strengths, which limited their biomedical applications, whereas the incorporation of the rigid AT structure successfully overcame this problem. By varying AT content in material synthesis, BLPAT materials with robust and tunable mechanical properties can be developed. Therefore, BLPATs may be used in diversified applications, from soft tissues, such as skin and nerve, to hard tissues, such as tooth and bone.<sup>[45–47]</sup>

#### 2.5. Fluorescence and PA Properties of BLPAT Pre-polymers

Fluorescence and PA properties of BLPAT pre-polymers were explored to confirm their applicability as dual functional imaging agents. The fluorescence spectra of BPLP and BLPAT pre-polymer solutions at different concentrations (5, 2.5, 1.25, 0.625, and 0.3125 mg mL<sup>-1</sup>) were tested (Figure S2a, Supporting Information). The dark color introduced by AT caused strong light absorption. Therefore, at the same pre-polymer concentration, the fluorescence intensities of BLPAT pre-polymer solutions were generally

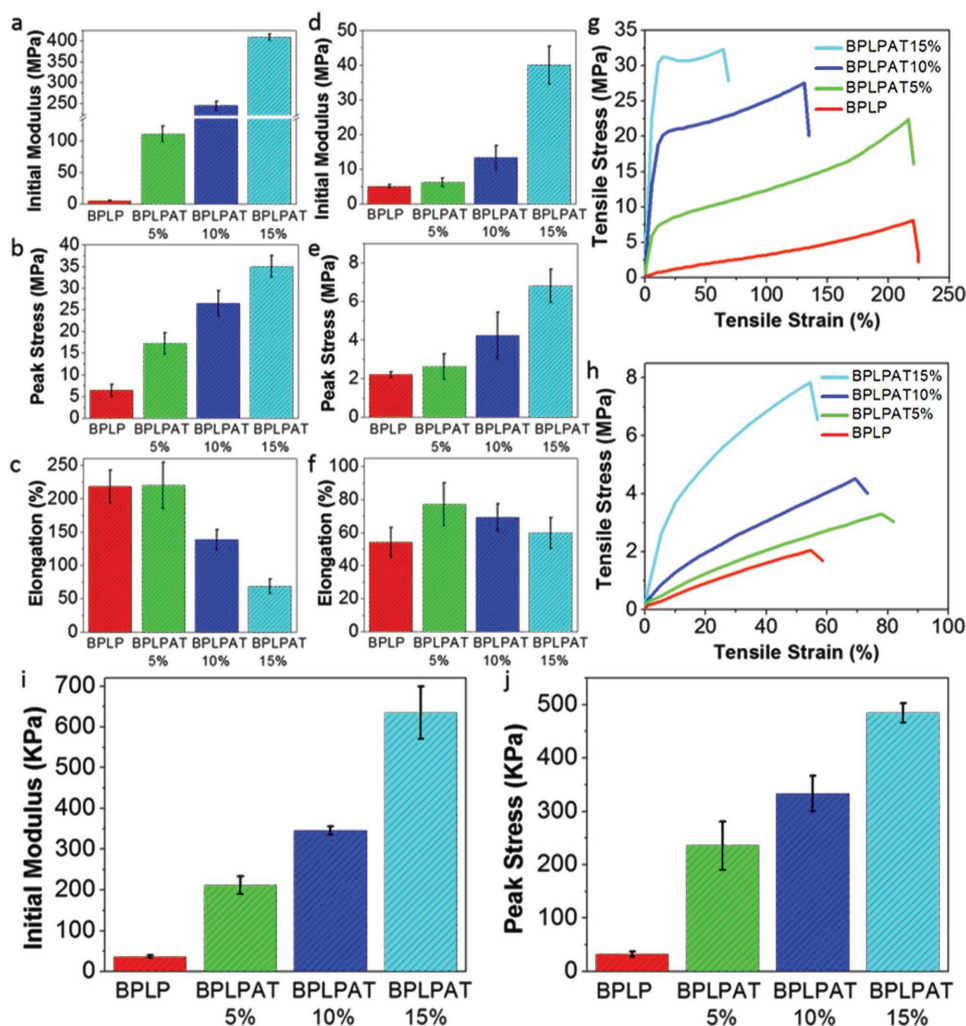


**Figure 3.** Mechanical properties of BPLPAT films and scaffolds. a) Initial modulus, b) peak stress, and c) elongation of BPLP and BPLPAT films under dry condition. d) Initial modulus, e) peak stress, and f) elongation of BPLP and BPLPAT films under wet condition. g) Tensile–strain curves of BPLP and BPLPAT films under wet condition. h) Tensile–strain curves of BPLP and BPLPAT scaffolds under wet condition.

lower than that of BPLP, and decreased with increased ratios of AT/CA (Figure S2b, Supporting Information). Notably, the fluorescence intensity of BPLPAT solutions reached a maximum within the testing concentration range (BPLPAT5% ( $1.25 \text{ mg mL}^{-1}$ ), BPLPAT10% ( $1.25 \text{ mg mL}^{-1}$ ), and BPLPAT15% ( $0.625 \text{ mg mL}^{-1}$ )), while the fluorescence intensity of BPLP solutions increased gradually with increasing concentrations under the same testing condition (Figure S2b, Supporting Information). For BPLP solutions, the increased concentrations caused higher fluorophore density but no significant changes of solution color, so higher concentrations had stronger fluorescence intensity compared to less concentrated solutions. In BPLPAT solutions, the increased concentrations not only resulted in densified fluorophores, but also led to more light absorption by the increasingly dark solutions, leading to optimal concentrations for maximum fluorescence intensity. To better understand the fluorescence differences between BPLP and BPLPATs, the fluorescence spectra of BPLP and BPLPAT solutions at a

concentration of  $1.25 \text{ mg mL}^{-1}$  were compared (Figure 4a), which intuitively presents decreased fluorescence intensity with the increase of AT content. In addition, the photostabilities of BPLP and BPLPAT pre-polymer solutions were studied (Figure S2c, Supporting Information), and the results exhibited a decreased photostability of BPLPATs with increased AT content. The fluorescence intensity of BPLP went down by less than 3% after UV light illumination for 3 h, while the intensity of BPLPAT15% decreased about 8%. However, all BPLPAT groups were much more stable than the Rhodamine B control, which decreased 25% in intensity.

PA imaging, based on the absorption of optical energy to generate acoustic signals, has significant advantages such as high spatial resolution, deep tissue penetration, high contrast, and nonionizing radiation.<sup>[30–32]</sup> Therefore, the PA imaging performance of BPLPATs was next investigated under variable wavelengths (680–920 nm). The quantitative comparison of the PA signal intensities of BPLPAT solutions at different concentrations is shown in Figure 4b. Due to their strong light absorption

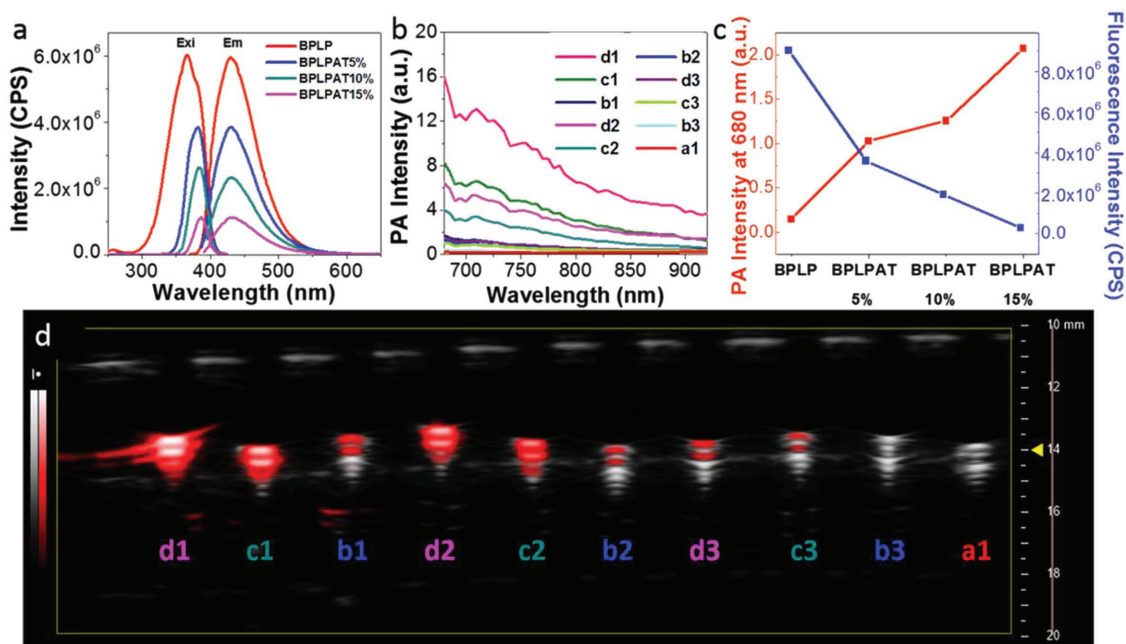


**Figure 4.** Fluorescence and PA properties of BPLPAT pre-polymer solutions. a) Fluorescence intensity spectra of BPLP and BPLPAT pre-polymers in dioxane at  $1.25 \text{ mg mL}^{-1}$ . b) PA intensity of BPLP and BPLPAT pre-polymer solutions in dioxane at various concentrations (5, 2.5,  $0.625 \text{ mg mL}^{-1}$ ). c) PA intensity and fluorescence intensity comparison of BPLP and BPLPAT solutions at  $2.5 \text{ mg mL}^{-1}$ . d) Representative superimposed ultrasound (gray-scale) and PA (pseudo-red scale) images of BPLP and BPLPAT pre-polymer solutions at various concentrations (BPLPAT15%  $5 \text{ mg mL}^{-1}$  (d1), BPLPAT10%  $5 \text{ mg mL}^{-1}$  (c1), BPLPAT5%  $5 \text{ mg mL}^{-1}$  (b1), BPLPAT15%  $2.5 \text{ mg mL}^{-1}$  (d2), BPLPAT10%  $2.5 \text{ mg mL}^{-1}$  (c2), BPLPAT5%  $2.5 \text{ mg mL}^{-1}$  (b2), BPLPAT15%  $0.625 \text{ mg mL}^{-1}$  (d3), BPLPAT10%  $0.625 \text{ mg mL}^{-1}$  (c3), BPLPAT5%  $0.625 \text{ mg mL}^{-1}$  (b3), BPLP  $5 \text{ mg mL}^{-1}$  (a1)).

at the PA testing wavelengths, BPLPAT pre-polymer solutions (BPLPAT5%, BPLPAT10%, and BPLPAT15%) presented distinct PA signals that increased with increased AT ratios and solution concentrations. By contrast, BPLP solutions had poor PA imaging performance, with even the highest solution concentration of  $5 \text{ mg mL}^{-1}$  presenting no significant PA signal. Within the testing wavelength range, BPLPAT pre-polymer solutions had the strongest PA intensity at the excitation wavelength of  $680 \text{ nm}$ . Representative superimposed ultrasound and PA images of BPLP and BPLPAT pre-polymer solutions at  $680 \text{ nm}$  are shown in Figure 4d, and are consistent with the quantitative comparison results (Figure 4b) wherein BPLPAT pre-polymers containing the highest proportion of AT (BPLPAT15%) and at highest concentration ( $5 \text{ mg mL}^{-1}$ ) exhibited the strongest PA signal.

To further understand the fluorescence and PA dual-imaging properties of BPLPATs, we compared the fluorescence intensity and PA intensity of BPLPAT pre-polymer solutions at the same concentration of  $2.5 \text{ mg mL}^{-1}$  (Figure 4c). The fluorescence intensity of BPLPAT solutions decreased with increasing AT content, while their respective PA signals increased gradually. Therefore, the introduction of AT in BPLPATs appears to sacrifice the fluorescence properties (intensity and photostability) to some degree, while enhancing PA imaging in a dose dependent manner. Thus, BPLPATs demonstrated excellent tunability on their dual-imaging properties through molecular design of materials, which enables custom-designing BPLPAT materials based on the required penetration depth, resolution, and sensitivity for different applications.

## 2.6. Imaging and Photothermal Capabilities of BPLPAT Nanoparticles

In addition to demonstrating powerful material structure and functionality modulation potential, BPLPATs were also amenable to various fabrication techniques, including fabrication into nanoparticles. Using the nanoprecipitation method,<sup>[48]</sup> BPLP, BPLPAT5%, BPLPAT10%, and BPLPAT15% nanoparticles with sizes of  $164.3 \pm 6.9$ ,  $178.2 \pm 4.3$ ,  $182.6 \pm 2.0$ , and  $181.9 \pm 5.7 \text{ nm}$  were prepared. All nanoparticles exhibited high stability, as demonstrated by their zeta potential values of  $-55.5 \pm 2.0$ ,  $-60.2 \pm 0.6$ ,  $-59.3 \pm 2.8$ , and  $-49.1 \pm 0.7 \text{ mV}$ , respectively (Table S2, Supporting Information).

BPLP and BPLPAT nanoparticle cellular uptake by PC-12 cells was conducted to investigate their fluorescence imaging and cell labeling capabilities. The fluorescent images of PC-12 cells with BPLP and BPLPAT nanoparticles were recorded with a fluorescence microscope (Figure 5a). Although BPLPATs had decreased fluorescence intensity compared to BPLP, cells stained with different nanoparticles all presented strong fluorescence. In addition, cells can be imaged with blue, green, and red fluorescence with different excitations, making BPLPAT nanoparticles versatile for cell labeling and imaging.

The PA imaging ability of BPLP and BPLPAT nanoparticles was also studied. In the PA imaging experiment, nanoparticle solutions with different concentrations were first placed in NIR-inactive polyurethane tubes, kept inside the water medium, to obtain quantitative signal intensities at wavelengths ranging from  $680$  to  $920 \text{ nm}$ . The PA intensities of nanoparticle solutions decreased with decreased AT

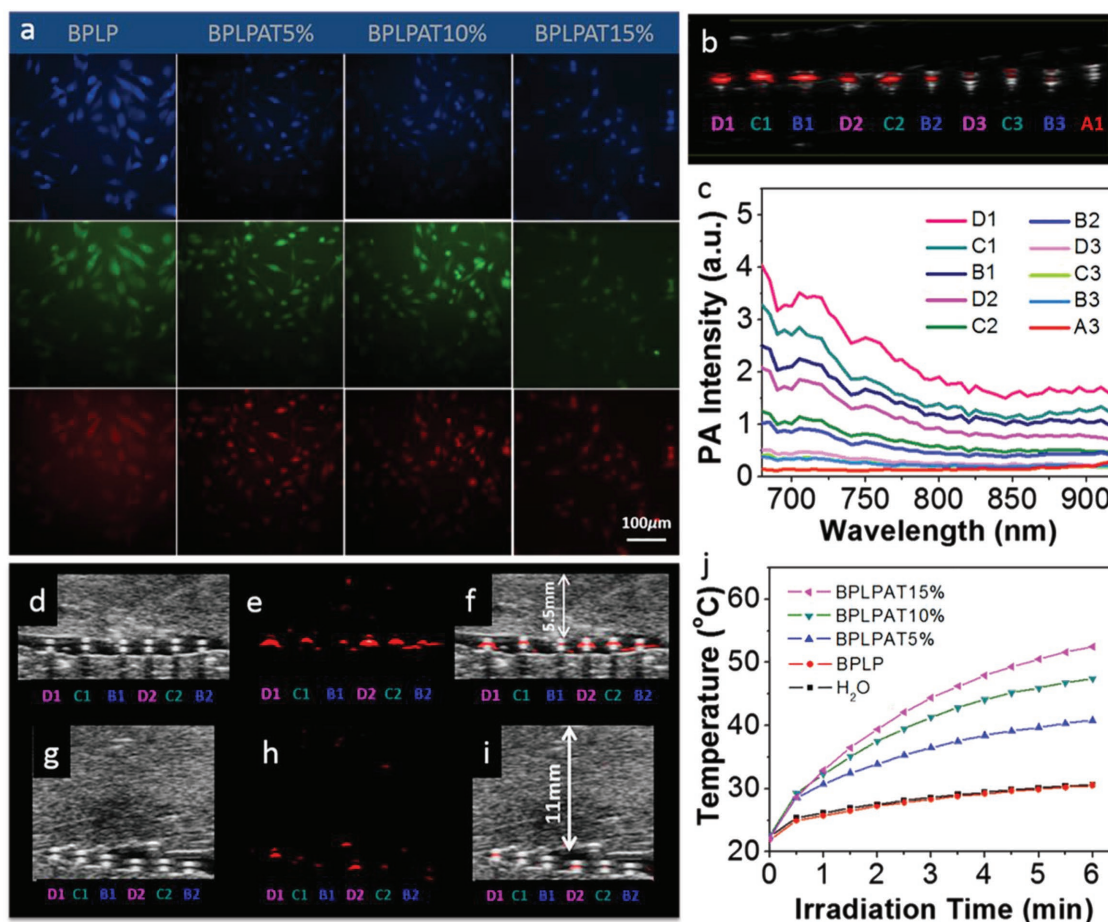


**Figure 5.** Fluorescence imaging, PA imaging, and photothermal capabilities of BPLPAT nanoparticles. a) Fluorescent images of PC12 cells uptaken with BPLP and BPLPAT nanoparticles with blue, green, and red fluorescence. b) Superimposed ultrasound and PA images of BPLP and BPLPAT nanoparticle solutions in plastic tubes in water medium at various concentrations. c) PA intensity of BPLP and BPLPAT nanoparticle solutions at various concentrations. d) Ultrasound images, e) PA images, and f) superimposed ultrasound and PA images of BPLP and BPLPAT nanoparticles under a 5.5 mm thick layer of chicken breast tissue. g) Ultrasound images, h) PA images, and i) superimposed ultrasound and PA images of BPLP and BPLPAT nanoparticles covered under a 11 mm thick layer of chicken breast tissue. j) Temperature rise traces of the BPLP and BPLPAT nanoparticles at a concentration of  $0.5 \text{ mg mL}^{-1}$  under NIR illumination, DI water works as the control (BPLPAT15%  $2 \text{ mg mL}^{-1}$  (D1), BPLPAT10%  $2 \text{ mg mL}^{-1}$  (C1), BPLPAT5%  $2 \text{ mg mL}^{-1}$  (B1), BPLPAT15%  $1 \text{ mg mL}^{-1}$  (D2), BPLPAT10%  $1 \text{ mg mL}^{-1}$  (C2), BPLPAT5%  $1 \text{ mg mL}^{-1}$  (B2), BPLPAT15%  $0.5 \text{ mg mL}^{-1}$  (D3), BPLPAT10%  $0.5 \text{ mg mL}^{-1}$  (C3), BPLPAT5%  $0.5 \text{ mg mL}^{-1}$  (B3), BPLP  $2 \text{ mg mL}^{-1}$  (A1)).

content and decreased concentrations of each nanoparticle group (Figure 5c; Figure S3a, Supporting Information). The representative superimposed ultrasound and PA images are presented in Figure 5b, further confirming the above quantitative results. Ex vivo deep tissue PA imaging of BPLP and BPLPAT nanoparticles was also conducted with chicken breast tissue (Figure 5d–i). BPLPAT5%, BPLPAT10%, and BPLPAT15% nanoparticle solutions at concentrations of 1 and  $2 \text{ mg mL}^{-1}$  demonstrated excellent PA imaging performance, when imaged through a 5.5 mm thick layer of chicken tissue (Figure 5e). When the thickness of the tissue was increased to 11 mm, BPLPAT15% nanoparticle solutions still showed strong PA signals at both concentrations, BPLPAT10% group presented decreased but detectable signals at both concentrations, whereas the PA signals of BPLPAT5% at both concentrations decreased significantly and were almost undetectable. BPLPAT nanoparticles were able to reach a penetration depth of centimeters, and the depth increased with AT content.

In situ thermal ablation is a promising cancer treatment technique in which material mediated local temperature increases are utilized to kill tumor cells following NIR irradiation. The high NIR absorbance of our BPLPAT materials suggested their potential for photothermal therapy. We thus evaluated the time-dependent temperature of our materials as a function of NIR irradiation time (Figure 5j). The original temperature was  $22 \text{ }^\circ\text{C}$ , while after irradiation for 6 min, the temperatures of  $0.5 \text{ mg mL}^{-1}$  of BPLPAT nanoparticle solutions increased dramatically (BPLPAT5% ( $40.8 \text{ }^\circ\text{C}$ ), BPLPAT10% ( $47.4 \text{ }^\circ\text{C}$ ), and BPLPAT15% ( $52.5 \text{ }^\circ\text{C}$ )), while that of BPLP only increased to  $30.5 \text{ }^\circ\text{C}$ , equivalent to deionized (DI) water ( $30.6 \text{ }^\circ\text{C}$ ). In this study, obvious AT content dependent temperature increases of BPLPAT nanoparticles were found under laser irradiation, whereas BPLP nanoparticle solution and pure water showed little change.

Therefore, BPLPAT nanoparticles not only have fluorescence and PA dual imaging properties, but also provide high

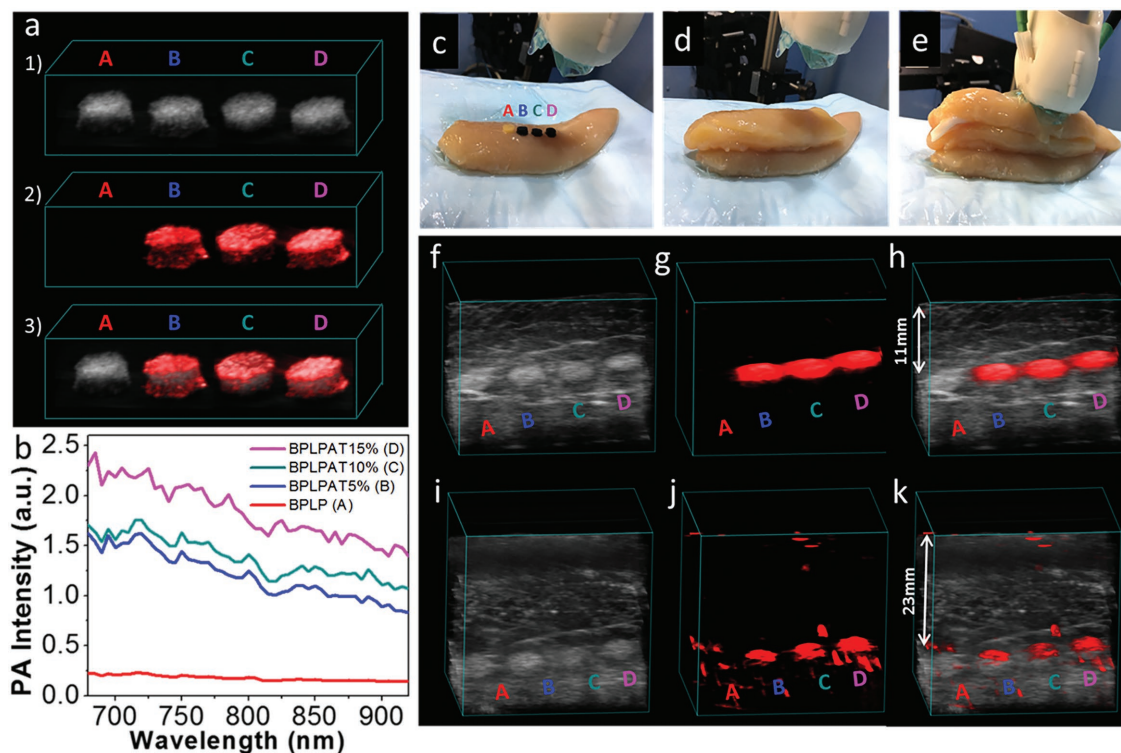


**Figure 6.** PA imaging of BLP and BLPAT scaffolds. a) (1) Ultrasound images, (2) PA images, and (3) superimposed ultrasound and PA images of BLP and BLPAT scaffolds embedded inside agar gel. b) PA intensity of BLP and BLPAT scaffolds. c–e) Experiment setup for deep tissue PA imaging of BLP and BLPAT scaffolds. f) Ultrasound images, g) PA images, and h) superimposed ultrasound and PA images of BLP and BLPAT scaffolds covered under a  $\approx 11$  mm thick layer of chicken breast tissue. i) Ultrasound images, j) PA images, and k) superimposed ultrasound and PA images of BLP and BLPAT scaffolds covered under two layers thick (total  $\approx 23$  mm thick) of chicken breast tissue.

NIR absorbance coefficients and excellent photothermal performance, rendering promising nanomaterials for cell labeling and cancer thermal treatments.

## 2.7. Imaging Capabilities of BLPAT Scaffolds

The salt leaching method was applied to fabricate cylindrical BLP and BLPAT scaffolds with a diameter of 7 mm, thickness of 3 mm, and interconnected porosity. To obtain their quantitative PA signals, BLP, BLPAT5%, BLPAT10%, and BLPAT15% scaffolds were embedded inside a piece of agar gel. PA intensities of BLPAT scaffolds were recorded at wavelengths from 680 to 920 nm (Figure 6b), and PA intensities at 680 nm were quantitatively compared (Figure S3b, Supporting Information). Scaffolds with higher AT content exhibit higher PA intensities (BLPAT15% > BLPAT10% > BLPAT5% > BLP). In Figure 6a, 3D structures from ultrasound images (Figure 6a1), PA images (Figure 6a2), as well as their superimposed images (Figure 6a3) are displayed. BLP scaffolds showed no noticeable PA signal, while all BLPAT scaffolds exhibited strong PA images with high contrast. To explore the deep tissue PA imaging capacity of BLPAT scaffolds, the BLP, BLPAT5%, BLPAT10%, and BLPAT15% scaffolds were imaged through an  $\approx 11$  mm and an  $\approx 23$  mm thick chicken breast tissue under 680 nm laser irradiation (Figure 6c–e). In both experiments, ultrasound

contrast of the scaffolds is poor due to lack of mechanical impedance mismatch between the scaffolds and surrounding tissue, highlighting a common disadvantage of ultrasound to image soft biological tissue material (Figure 6f,i). However, the BLPAT5%, BLPAT10%, and BLPAT15% scaffolds provided excellent 3D PA images without any background noise under a  $\approx 11$  mm chicken tissue (Figure 6g). The PA imaging performance of BLPAT scaffolds declined under a  $\approx 23$  mm of chicken tissue (Figure 6j) with some background signals. The superimposed images of volumetric ultrasound and PA images (Figure 6h,k) of whole scaffolds are clearly presented for BLPAT5%, BLPAT10%, and BLPAT15%. Using fluorescence imaging, it is difficult to achieve high resolution and high optical contrast images with such deep penetration depths (greater than 1 cm); however, with strong absorption of light in the NIR spectral range, BLPAT scaffolds were able to generate high optical contrast PA imaging, which provided penetration depth extending to more than 2 cm. In addition, because the differences in optical absorption between materials and surrounding tissues are much larger than those in acoustic impedance, PA imaging offered greater contrast and specificity of materials from surrounding tissues compared to ultrasound imaging. With excellent PA imaging performance, BLPAT scaffolds may be applied as implant materials for versatile tissue regeneration applications where in situ monitoring of their location, degradation, and/or shape variations is desired.

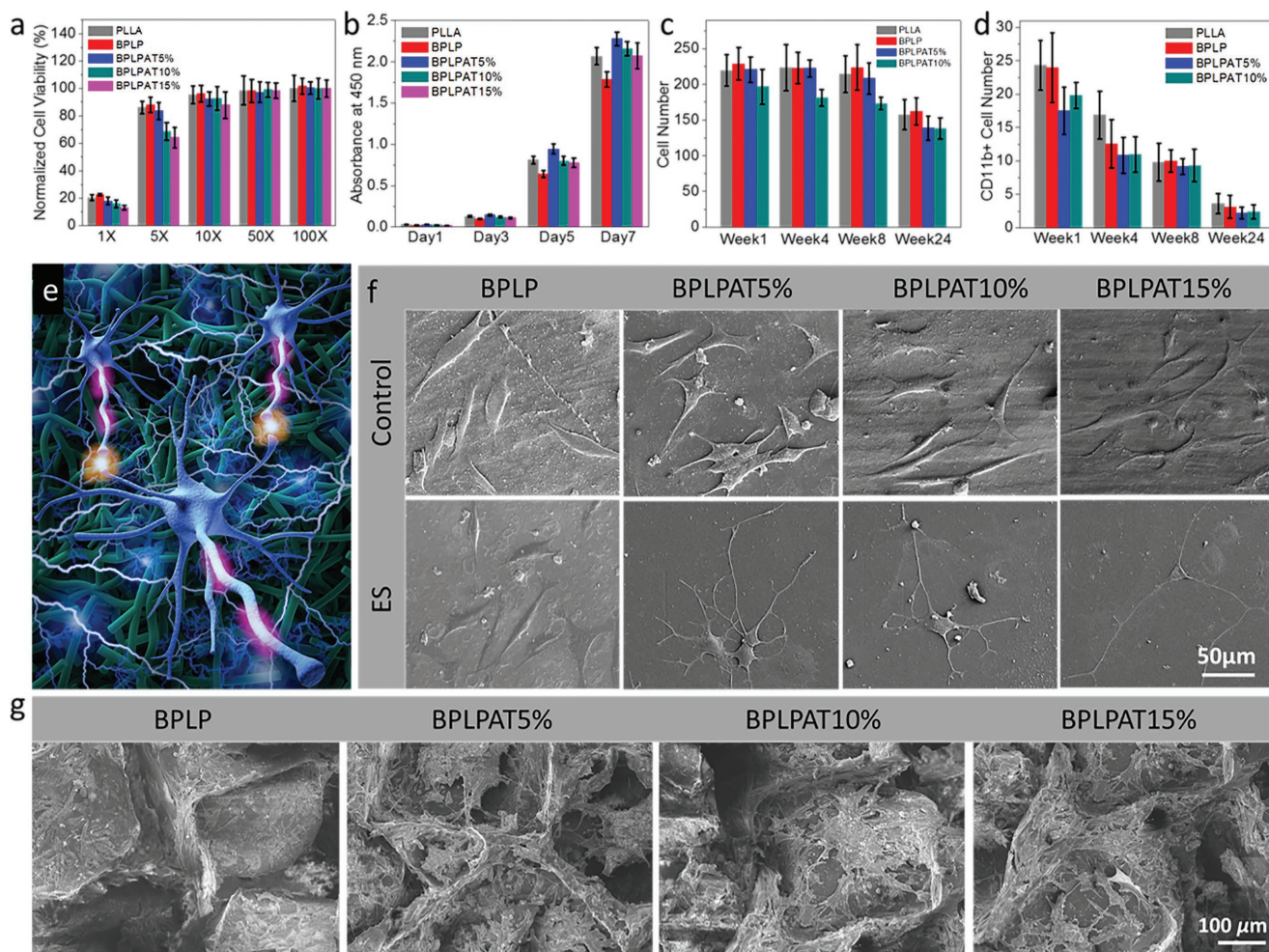


**Figure 7.** In vitro cell culturing and in vivo foreign body response studies on BPLPAT materials. a) Cytotoxicity of degradation products of BPLP and BPLPATs, PLLA film as a control. b) PC12 cell proliferation studies on BPLP and BPLPAT films for 7 d, PLLA film as a control. c) Averaged total and d) CD11b positive cell numbers in a  $200 \times 200 \mu\text{m}^2$  square region near the implant films. e) Schematic of electrical stimulation of PC-12 cells on cross-linked BPLPAT materials. f) SEM images of PC-12 cells on BPLP and BPLPAT films without electrical stimulation (control) and with electrical stimulation (ES). g) SEM images of PC-12 cells on BPLP and BPLPAT scaffolds with electrical stimulation.

### 2.8. In Vitro Cytotoxicity Evaluation

For any materials that are going to be used for in vivo applications, it is necessary to assess their toxicities. Therefore, in vitro cytotoxicity evaluation for degraded products of BPLP and BPLPAT10% with rat pheochromocytoma (PC-12) cells was conducted before in vivo evaluation (Figure 7a). Degradation products of polymers at various concentrations (1 $\times$ :  $10 \text{ mg mL}^{-1}$ ; 5 $\times$ :  $2 \text{ mg mL}^{-1}$ ; 10 $\times$ :  $1 \text{ mg mL}^{-1}$ ; 50 $\times$ :  $0.2 \text{ mg mL}^{-1}$ ; and 100 $\times$ :  $0.1 \text{ mg mL}^{-1}$ ) were tested. Poly(L-lactide) (PLLA) was used as control. At the highest concentration of  $10 \text{ mg mL}^{-1}$ , the degradation products from all groups (PLLA, BPLP, BPLPAT5%, BPLPAT10%, and BPLPAT15%) showed high toxicity, with cell viability of around (PLLA and BPLP) or lower than (BPLPAT5%, BPLPAT10%, and BPLPAT15%) 20%. When the concentration was reduced to  $2 \text{ mg mL}^{-1}$ , the cell viabilities of PLLA, BPLP, and BPLPAT5% groups were over 80%. BPLPAT10% and BPLPAT15% groups showed slightly lower cell viabilities of around 70%. However, when the concentration was reduced to  $1 \text{ mg mL}^{-1}$ , the cell viabilities of all testing groups were higher than 85%, which demonstrated that the diluted degradation products were

nontoxic. From the toxicity study, we can see that more incorporated AT caused higher cellular toxicity at very concentrated conditions; however, as shown above, BPLPATs only degrade slowly. The local concentrations of their degradation products are expected to remain in the safe window in vivo, which can be confirmed by the excellent in vivo host response data presented below.

### 2.9. In Vitro Cell Proliferation and Electrical Stimulation

In order to test the effects of electrical functionalities of BPLPAT materials on cellular activities, PC-12 cells were cultured on a series of BPLPAT films (BPLP, BPLPAT5%, BPLPAT10%, and BPLPAT15%) up to 7 d (Figure 7b). BPLPAT films significantly promoted the proliferation of PC-12 cells when compared with BPLP, which might be caused by the electroactive properties. However, with increased AT content, BPLPAT10% and BPLPAT15% films showed slightly reduced cell proliferation rate compared to BPLPAT5%, likely caused by the toxicity of more AT released over time. In vitro cell culture

studies confirmed the cytocompatibility of BPLPAT films, as well as their capability for the promotion of PC-12 proliferation.

Conductive materials are capable of transferring electrical signals among cells. Therefore, we applied electrical fields to BPLPAT films and investigated the differentiation behavior of the cultured PC-12 cells (Figure 7e). In this experiment, BPLP, BPLPAT5%, BPLPAT10%, and BPLPAT15% films were studied, and films without electrical stimulation were used as controls. After electrical stimulation, cell morphologies were studied with scanning electron microscope (SEM) (Figure 7f). Without electrical stimulation, PC-12 cells cultured on BPLP films mostly kept their original spindle shape, whereas cells on BPLPAT films formed multiple neurites along each cell body. The morphologies of PC-12 cells on BPLP films did not show obvious differences from those without electrical stimulation; however, cells on BPLPAT films changed dramatically after electrical stimulation evidenced by the long and branched neurites along their cell bodies. Therefore, BPLPAT films themselves were able to stimulate neurite formation due to their inherent electrical conductivity, and the addition of external electrical stimulation strongly promoted the growth and elongation of neurites. BPLP, BPLPAT5%, BPLPAT10%, and BPLPAT15% scaffolds were also used for PC-12 cell growth and differentiation under electrical stimulation. SEM images show that PC-12 cells were able to cover the surface and penetrate deep into the porous scaffold (Figure 7g). Moreover, the branched and extended neurites indicate that cells that grew on BPLPAT scaffolds displayed improved differentiation. Therefore, BPLPAT scaffolds will be great candidates for nerve regeneration applications.

### 2.10. In Vivo Foreign Body Response Studies on BPLPAT Films

In vivo foreign body response of BPLPAT films was studied via a subcutaneous implantation study of BPLP, BPLPAT5%, and BPLPAT10% in Sprague Dawley (SD) rats using PLLA as control. All samples implanted for 1 week produced a slight acute inflammatory response, expected with the introduction of a foreign material into the body and confirmed by cell infiltration (H & E staining, Figure S4, Supporting Information) as well as the appearance of CD11b positive cells (CD11b staining, Figure S5, Supporting Information) in the tissues surrounding the polymer films. After 8 weeks of implantation, a thin fibrous capsule between all sample films and muscle was formed, indicating minimal inflammatory reactions. Quantitative cell counting study indicated that total cell densities and CD11b positive cell densities surrounding different polymer film implants declined over time (Figure 7c,d). Interestingly, BPLPAT5% and BPLPAT10% films exhibited less total cell densities and CD11b positive cell densities at each time point. After 24 weeks of implantation, most of the cells surrounding the implanted samples were fibroblast cells. CD11b positive cells were rarely seen after 24 weeks, indicating that minor chronic inflammatory reaction took place and the degradation products over time did not cause noticeable toxicity. The mild inflammatory response suggested that BPLPAT films and their degradation products present more favorable host responses than the controls, BPLP and PLLA. These studies demonstrated that BPLPAT materials are biocompatible and safe as implant materials or devices for long-term in vivo applications.

## 3. Conclusion

In this study, we developed a biodegradable multifunctional citrate-based biomaterial, BPLPAT, through a facile and efficient polycondensation reaction. The obtained BPLPAT materials demonstrated intrinsic dual-modal fluorescence/PA imaging capability, electrical conductivity, tunable mechanical properties, and programmable degradation profiles. BPLPAT polymers were fabricated into films, scaffolds, and nanoparticles exemplify their excellent processability. Dual imaging capabilities enabled detection of BPLPAT nanoparticles as well as 3D imaging for BPLPAT scaffolds under deep tissue. BPLPAT nanoparticles demonstrated great photothermal performance due to their high NIR absorbance coefficient. Favorable electroactivity successfully enabled BPLPAT films and scaffolds to promote proliferation and differentiation of PC-12 cells. It is our belief that the unique combination of material properties in one setting including fluorescence imaging and labeling of cells, PA imaging, and electroactivity of the fully degradable BPLPAT makes the polymer an enabling tool for diversified biomedical and biological applications including tissue engineering, imaging, drug delivery, and cancer treatment. Furthermore, the citrate-based biomaterial platform is able to incorporate versatile functional chemicals, biological molecules, or drugs to fulfill specific medical requirements, serving as a powerful tool to enable more personalized and effective medical treatments.

## Supporting Information

Supporting Information is available from the Wiley Online Library or from the author.

## Acknowledgements

The authors would like to acknowledge financial support from National Institutes of Health (USA) awards (grant nos. CA182670, EB024829, and AR072731 to J.Y.; grant no. EB017729 to S.R.K), National Natural Science Foundation of China (grant no. 81460210 to D.L.; grant no. 81460173 to L.G.; grant no. 81560050 to L.S.), and Department of Science and Technology of Yunnan Province (grant no. 2017FA035 to D.L.; grant no. 2017FE467(-008) to L.S.). The authors also thank Fuji-VisualSonics and its technical team (Andrew Heinmiller and Kelly O'Connell) for their help with photoacoustic imaging experiments. Animal experiments were performed according to protocols approved by the Institutional Animal Care and Use Committee (IACUC) at the Pennsylvania State University.

## Conflict of Interest

The authors declare no conflict of interest.

## Keywords

citrate, conductive polymers, degradation, fluorescence, photoacoustic imaging

Received: March 12, 2018

Revised: May 27, 2018

Published online:

- [1] N. A. Peppas, R. Langer, *Science* **1994**, 263, 1715.
- [2] R. Langer, D. A. Tirrell, *Nature* **2004**, 428, 487.
- [3] N. Huebsch, D. J. Mooney, *Nature* **2009**, 462, 426.
- [4] M. J. Webber, O. F. Khan, S. A. Sydlík, B. C. Tang, R. Langer, *Ann. Biomed. Eng.* **2015**, 43, 641.
- [5] M. J. Webber, E. A. Appel, E. W. Meijer, R. Langer, *Nat. Mater.* **2016**, 15, 13.
- [6] D. J. Mooney, M. Darnell, *Nat. Mater.* **2017**, 16, 6365.
- [7] R. T. Tran, J. Yang, G. A. Ameer, *Annu. Rev. Mater. Res.* **2015**, 45, 277.
- [8] C. Ma, E. Gerhard, Q. Lin, S. Xia, A. D. Armstrong, J. Yang, *Bioactive Mater.* **2018**, 3, 19.
- [9] J. Guo, Z. Xie, R. T. Tran, D. Xie, D. Jin, X. Bai, J. Yang, *Adv. Mater.* **2014**, 26, 1906.
- [10] D. Shan, C. Zhang, S. Kalaba, N. Mehta, G. B. Kim, Z. Liu, J. Yang, *Biomaterials* **2017**, 143, 142.
- [11] J. Guo, G. B. Kim, D. Shan, J. P. Kim, J. Hu, W. Wang, F. G. Hamad, G. Qian, E. B. Rizk, J. Yang, *Biomaterials* **2017**, 112, 275.
- [12] J. Guo, W. Wang, J. Hu, D. Xie, E. Gerhard, M. Nisic, D. Shan, G. Qian, S. Zheng, J. Yang, *Biomaterials* **2016**, 85, 204.
- [13] R. van Lith, E. K. Gregory, J. Yang, M. R. Kibbe, G. A. Ameer, *Biomaterials* **2014**, 35, 8113.
- [14] J. Yang, Y. Zhang, S. Gautam, L. Liu, J. Dey, W. Chen, R. P. Mason, C. A. Serrano, K. A. Schug, L. Tang, *Proc. Natl. Acad. Sci. USA* **2009**, 106, 10086.
- [15] J. Hu, J. Guo, Z. Xie, D. Shan, E. Gerhard, G. Qian, J. Yang, *Acta Biomater.* **2016**, 29, 307.
- [16] Z. Xie, Y. Zhang, L. Liu, H. Weng, R. P. Mason, L. Tang, K. T. Nguyen, J. T. Hsieh, J. Yang, *Adv. Mater.* **2014**, 26, 4491.
- [17] D. Xie, J. Guo, M. R. Mehdizadeh, R. T. Tran, R. Chen, D. Sun, G. Qian, D. Jin, X. Bai, J. Yang, *J. Mater. Chem.* **2015**, 3, 387.
- [18] L. C. Su, H. Xu, R. T. Tran, Y. T. Tsai, L. Tang, S. Banerjee, J. Yang, K. T. Nguyen, *ACS Nano* **2014**, 8, 10826.
- [19] J. Li, Y. Tian, D. Shan, A. Gong, L. Zeng, W. Ren, L. Xiang, E. Gerhard, J. Zhao, J. Yang, A. Wu, *Biomaterials* **2017**, 116, 106.
- [20] J. P. Kim, Z. Xie, M. Creer, Z. Liu, J. Yang, *Chem. Sci.* **2017**, 8, 550.
- [21] C. Zhang, J. P. Kim, M. Creer, J. Yang, Z. Liu, *Biosens. Bioelectron.* **2017**, 97, 164.
- [22] X. Michalet, F. F. Pinaud, L. A. Bentolila, J. M. Tsay, S. Doose, J. J. Li, G. Sundaresan, A. M. Wu, S. S. Gambhir, S. Weiss, *Science* **2005**, 307, 538.
- [23] R. Weissleder, *Nat. Biotechnol.* **2001**, 19, 316.
- [24] N. Artzi, N. Oliva, C. Puron, S. Shitreet, S. Artzi, A. Bon Ramos, A. Groothuis, G. Sahagian, E. R. Edelman, *Nat. Mater.* **2011**, 10, 704.
- [25] Z. Fan, L. Sun, Y. Huang, Y. Wang, M. Zhang, *Nat. Nanotechnol.* **2016**, 11, 388.
- [26] T. L. Sita, F. M. Kouri, L. A. Hurley, T. J. Merkel, A. Chalastanis, J. L. May, S. T. Ghelfi, L. E. Cole, T. C. Cayton, S. N. Barnaby, A. J. Sprangers, N. Savalia, C. D. James, A. Lee, C. A. Mirkin, A. H. Stegh, *Proc. Natl. Acad. Sci. USA* **2017**, 114, 4129.
- [27] L. Cheng, J. Liu, X. Gu, H. Gong, X. Shi, T. Liu, C. Wang, X. Wang, G. Liu, H. Xing, W. Bu, B. Sun, Z. Liu, *Adv. Mater.* **2014**, 26, 1886.
- [28] E. S. Olson, T. Jiang, T. A. Aguilera, Q. T. Nguyen, L. G. Ellies, M. Scadeng, R. Y. Tsien, *Proc. Natl. Acad. Sci. USA* **2010**, 107, 4311.
- [29] K. Li, B. Liu, *Chem. Soc. Rev.* **2014**, 43, 6570.
- [30] H. J. Knox, J. Hedhli, J. Chan, K. Khalili, L. W. Dobrucki, T. W. Kim, *Nat. Commun.* **2017**, 8, 1794.
- [31] H. Moon, D. Kumar, H. Kim, C. Sim, J. H. Chang, J. M. Kim, H. Kim, D. K. Lim, *ACS Nano* **2015**, 9, 2711.
- [32] K. Pu, A. J. Shuhendler, J. V. Jokerst, J. Mei, S. S. Gambhir, Z. Bao, J. Rao, *Nat. Nanotechnol.* **2014**, 9, 233.
- [33] J. Wang, R. Yan, F. Guo, M. Yu, F. Tan, N. Li, *Nanotechnology* **2016**, 27, 0957.
- [34] X. Liang, Y. Li, X. Li, L. Jing, Z. Deng, X. Yue, C. Li, Z. Dai, *Adv. Funct. Mater.* **2015**, 25, 1451.
- [35] N. K. Guimard, N. Gomez, C. E. Schmidt, *Prog. Polym. Sci.* **2007**, 32, 876.
- [36] T. H. Qazi, R. Rai, A. R. Boccaccini, *Biomaterials* **2014**, 35, 9968.
- [37] D. Uppalapati, B. J. Boyd, S. Garg, J. Travas-Sejdic, D. Svirskis, *Biomaterials* **2016**, 111, 149.
- [38] G. Yang, K. L. Kampstra, M. R. Abidian, *Adv. Mater.* **2014**, 26, 4954.
- [39] B. Guo, L. Glavas, A. C. Albertsson, *Prog. Polym. Sci.* **2013**, 38, 1263.
- [40] M. Xie, L. Wang, B. Guo, Z. Wang, Y. E. Chen, P. X. Ma, *Biomaterials* **2015**, 71, 158.
- [41] Y. Wu, L. Wang, B. Guo, Y. Shao, P. X. Ma, *Biomaterials* **2016**, 87, 18.
- [42] K. G. Neoh, E. T. Kang, S. H. Khor, K. L. Tan, *Polym. Degrad. Stab.* **1990**, 27, 107.
- [43] Z. A. Boeva, V. G. Sergeev, *Polym. Sci., Ser. C* **2014**, 56, 144.
- [44] H. J. Sung, C. Meredith, C. Johnson, Z. S. Galis, *Biomaterials* **2004**, 25, 5735.
- [45] G. A. Holzapfel, *The Handbook of Materials Behavior Models*, Academic Press, Boston, MA, USA **2001**, 3, 1049.
- [46] G. Osterhoff, E. F. Morgan, S. J. Shefelbine, L. Karim, L. M. McNamara, P. Augat, *Injury* **2016**, 47, S11.
- [47] Y. C. Fung, *Biomechanics: mechanical properties of living tissues*, Springer Science & Business Media, New York, NY, USA **2013**.
- [48] Y. Zhang, R. T. Tran, I. S. Qattan, Y. T. Tsai, L. Tang, C. Liu, J. Yang, *Biomaterials* **2013**, 34, 4048.

# ADVANCED FUNCTIONAL MATERIALS

## Supporting Information

for *Adv. Funct. Mater.*, DOI: 10.1002/adfm.201801787

Development of Citrate-Based Dual-Imaging Enabled  
Biodegradable Electroactive Polymers

*Dingying Shan, Sri-Rajasekhar Kothapalli, Dino J. Ravnice,  
Ethan Gerhard, Jimin P. Kim, Jinshan Guo, Chuying Ma,  
Jiazhi Guo, Li Gui, Lin Sun, Di Lu,\* and Jian Yang\**

## Supporting Information

**Title** Development of Citrate-based Dual-Imaging Enabled Biodegradable Electroactive Polymers

*Dingying Shan, Sri-Rajasekhar Kothapalli, Dino J. Ravnic, Ethan Gerhard, Jimin P. Kim, Jinshan Guo, Chuying Ma, Jiazhi Guo, Li Gui, Lin Sun, Di Lu\*, Jian Yang\**

### Experimental Section

*Materials:* All chemicals were purchased from Sigma-Aldrich, and were used as received without further purification, except where otherwise noted.

*Synthesis of BPLPAT Pre-polymers:* a) Synthesis of aniline tetramer (AT): Aniline tetramer (AT) was synthesized with the following steps. First, N-phenyl-1,4-phenylenediamine (3.6848 g, 0.02 mol) was dissolved in a mixture of acetone and 1 mol L<sup>-1</sup> HCl (V/V 160:160 mL) at 0 °C in an ice bath. Ammonium persulfate (APS) (4.564 g, 0.02 mol) in acetone/HCl solution was then added drop by drop to the above solution within 30 min with vigorous stirring. The reaction proceeded for 2 hrs. The mixture was filtered to collect AT, and the resultant AT was then washed with 1 mol L<sup>-1</sup> HCl and distilled water. Later, AT was de-doped in 1 mol L<sup>-1</sup> NH<sub>4</sub>OH for 2 hrs and filtered, and then washed until the filtrate was neutral. Finally, the AT was lyophilized for 24 hrs and stored in a drying chamber until further use. b) Synthesis of BPLPAT pre-polymers: BPLPAT pre-polymers were synthesized using a one-pot polycondensation reaction (Figure S1). Representatively, citric acid (CA), 1,8-octanediol (OD), L-cysteine, and AT at molar ratios of 1:1.2:0.2:0/0.05/0.10/0.15 were added to a round-bottom flask, and the reaction was carried out at 110 °C under nitrogen atmosphere for 5 hrs. The pre-polymer was dissolved in

1,4-dioxane and purified by precipitating the solution into distilled water. Finally, BPLPAT pre-polymers were lyophilized for 24 hrs and stored in a drying chamber until further use. According to the theoretical molar ratios of AT to CA, which were set as 0%, 5%, 10%, and 15%, the samples were herein referred to as BPLP, BPLPAT5%, BPLPAT10%, and BPLPAT15%, respectively.

*Preparation of BPLPAT Films, Nanoparticles, and Scaffolds:* BPLPATs exhibited excellent processability, enabling them to be fabricated into various forms, including films, nanoparticles, and interconnected porous scaffolds, for versatile applications. To prepare BPLPAT films, respective pre-polymers in dioxane were cast onto Teflon molds, followed by evaporation and thermal crosslinking at 100°C for 3 days. In this thermal process, un-reacted -COOH and -OH groups of BPLPAT pre-polymers are cross-linked into an elastomeric network. For nanoparticle preparation, BPLPAT (0.4 g) was dissolved in acetone (10 mL). The polymer solution was added dropwise to deionized water (20 mL) under magnetic stirring (600 rpm). The setup was left in a chemical hood for 6 hrs to evaporate acetone. Desired concentrations of nanoparticle solutions were achieved by either water evaporation or dilution. Polymer scaffolds were prepared by a traditional salt leaching method as described previously.<sup>[48]</sup>

*Structural Characterizations:* Attenuated total reflectance-Fourier transform infrared (ATR-FTIR) characterization was performed on a Bruker Vertex 70 FTIR spectrometer with a Pike Miracle Single-Bounce diamond crystal plate accessory at room temperature. FTIR spectra were recorded over a wavelength range of 400–4000  $\text{cm}^{-1}$ . Nuclear magnetic resonance ( $^1\text{H}$  NMR) spectra (300 MHz,  $\text{DMSO-}d_6$ ,  $\delta$ ) of polymers were recorded on a Bruker DPX-300 FT-NMR spectrometer.

*Electroactive Properties and Electrical Conductivity Measurements:* The UV-Vis spectra of BPLPAT pre-polymers and their camphorsulfonic acid (CSA)-doped and APS-doped solutions were recorded with a UV-2450 spectrophotometer. All samples were dissolved in DMSO at equivalent concentrations, and were doped with 1 mol L<sup>-1</sup> CSA and APS. Cyclic voltammetry (CV) was performed with an Autolab PGSTAT-302N in a conventional three-electrode system with a platinum wire as working electrode, a platinum foil as auxiliary electrode, and an Ag/AgCl reference electrode. Polymer solutions were in ethanol, and 1 mol L<sup>-1</sup> CSA was used for material doping. The scan rate was 50 mV s<sup>-1</sup> for all samples. A four-point probe (Jandel Engineering Ltd.) was used to measure the electrical conductivity of BPLPAT film (doped with CSA) at room temperature. The conductivity was calculated by the following formula:

$$R_b = 4.532(V/I)t, \quad \text{Equation (1)}$$

where  $R_b$  = Bulk resistivity (Ohm-cm),  $V$  = measured voltage (Volt),  $I$  = current setting (Ampere), and  $t$  = thickness of layer being measured in cm. The electrical conductivity was then calculated using the following equation:

$$\sigma = 1/R_b. \quad \text{Equation (2)}$$

*In vitro Degradation Studies of BPLPAT Pre-polymers and Films:* *In vitro* degradation was conducted with ~80 mg of BPLP and BPLPAT10% pre-polymers, as well as BPLP and BPLPAT10% films (thickness of 0.15-0.30 mm) placed in tubes containing 10 mL of phosphate buffered saline (PBS, pH=7.4) and incubated at 37°C. The samples were weighed before degradation to find the initial mass ( $W_0$ ). For pre-polymer degradation, PBS buffer was replaced daily to ensure a constant pH of 7.4. For crosslinked film samples, PBS buffer was replaced daily in the first week and weekly for subsequent weeks. At each desired time point, the samples were taken out and thoroughly washed with deionized water 3 times, and then lyophilized. Each

sample was weighed to find the remaining mass (Wt). Six parallel specimens were averaged, and the results are presented as means  $\pm$  standard deviation. The percent mass remaining was calculated based on the following equation:

$$\text{Mass Remaining (\%)} = (W_t/W_0) \times 100. \quad \text{Equation (3)}$$

*Mechanical Properties:* Mechanical testing was conducted according to the ASTM D412a standard on an Instron 5966 machine. For tensile testing, the Instron machine was equipped with a 500 N load cell. Polymer film samples (3 cm in length, 0.6 cm in width, and 200  $\mu\text{m}$  in thickness) under both dry and hydrated (immersed in PBS for 24hrs) conditions were tested. Samples were pulled until failure at a rate of 500  $\text{mm min}^{-1}$  to obtain stress–strain curves. The initial slope (0–10%) of the curve was used to determine the initial modulus of the samples. Compression testing was applied on polymer scaffold samples (7 mm in diameter, and 3mm in thickness). Samples were compressed until reaching 50% of the thickness at a rate of 1.3  $\text{mm min}^{-1}$  with a 1 kN load cell. Six specimens were averaged for each sample, and the results are presented as means  $\pm$  standard deviation.

*Fluorescence Properties:* All photoluminescence spectra were acquired on a HORIBA Scientific Fluoromax-4 spectrofluorometer. All pre-polymers were dissolved in 1,4-dioxane to test photoluminescence unless otherwise noted. Both the excitation and the emission slit widths were set at 2 nm. For photostability testing, pre-polymer solutions at concentrations of 0.625  $\text{mg mL}^{-1}$  were illuminated by continuous ultraviolet (UV) light for 3 hrs, with Rhodamine B serving as control.

*Photoacoustic (PA) Properties:* PA imaging studies were conducted using a commercial PA imaging system (Vevo LAZR, FUJIFILM VisualSonics, Toronto, Canada). To evaluate the PA properties of BPLPAT polymers and nanoparticles, the respective solutions were injected into

polyethylene (PE50) tubes and kept in the center of a water bath for imaging, while BPLPAT scaffolds were evaluated by embedding in 10% agar gel. To demonstrate deep tissue imaging capabilities, BPLPAT scaffolds/PE tubes filled with BPLPAT nanoparticle solutions were imaged through thick chicken breast tissue. A dedicated customer-designed transducer, which combines proven high-frequency (15 MHz center frequency) ultrasound imaging technology with an integrated fiber optic cable for high-energy laser light delivery in the wavelength range (680 to 920 nm), was used to generate PA images of all samples. PA images and intensities were analyzed using Vevo LAB software.

*Photothermal Properties:* In order to investigate the photothermal properties of BPLPAT nanoparticles, BPLP and BPLPAT nanoparticle solutions at concentrations of  $0.5 \text{ mg mL}^{-1}$  were exposed to an 808-nm NIR laser at a power density of  $1.5 \text{ W cm}^{-2}$  and solution temperature was monitored for 6 minutes, with DI water as a control.

*In vitro Cytotoxicity and Cell Proliferation Studies:* The cytotoxicity of degradation products was assessed by Cell Counting Kit-8 (CCK-8) assay against PC-12 Adh cells (ATCC® CRL-1721.1™). Poly(L-lactide) (PLLA) ( $M_n \sim 100,000$ ) was used as a control. Polymer films (1 g) were fully degraded in 10 mL of 2 M NaOH solution. The resultant degradation product solutions were adjusted to pH 7.4 with 1 M HCl solution and then diluted to 1×, 10× and 100× concentrations using PBS (pH 7.4). All the solutions were filtered through a sterilized  $0.22 \mu\text{m}$  filter prior to cell culturing. PC-12 cells were cultured in a surface treated  $25 \text{ cm}^2$  tissue culture flask with F-12K medium (Kaighn's Modification of Ham's F-12 Medium (ATCC® 30-2004™)) supplemented with 2.5% fetal bovine serum (FBS), 15% horse serum and 1% antibiotics. The cells were detached and suspended in media to obtain a seeding density of  $5 \times 10^4 \text{ cell mL}^{-1}$ . 200  $\mu\text{L}$  of the cell suspension was added into each well of 96-well plates. The cells were then

incubated at 37 °C, 5% CO<sub>2</sub> and 95% humidity for 24 hrs, followed by the addition of 20 µL of diluted degradation solutions into each well. After another 24 hrs, CCK-8 was applied to test cell viability. The cell viabilities of PC-12 cells in medium containing polymer degradation solutions were normalized to that of cells cultured in normal medium. To test the cytotoxicity of polymer films, films were cut into disks to fit 96 well plates. The films were sterilized by treating with 70% ethanol, UV light, and culture medium in sequence, then placed on the bottom of 96-well plates. To each well, 200 µL of cell suspensions (at  $1 \times 10^4$  cells mL<sup>-1</sup>) in culturing media were added, and CCK-8 was applied to test cell viability at time points of 1, 3, 5, and 7 days to study PC-12 proliferation.

*Cell Uptake and Fluorescence Labeling:* The cell uptake of BPLP and BPLPAT nanoparticles was examined *in vitro* using fluorescence imaging. 1 mL of PC-12 cell suspension (5,000 cells mL<sup>-1</sup>) was added into each well of 24 well plates. Following 24 hrs incubation, media was then aspirated and the cells were washed three times with PBS. After 4 hrs of incubation with BPLPAT nanoparticles (10 mg mL<sup>-1</sup> in PBS), the nanoparticle suspension was aspirated and the cells were washed three times with PBS to remove the excess nanoparticles. The cells were fixed with 4% paraformaldehyde for 2 hrs. After fixing, cells were mounted and imaged under a Leica DMLP fluorescence microscope (Leica Microsystems, Bannockburn, IL) equipped with a Nikon E500 Camera (8.4V, 0.9A, Nikon Corp., Japan).

*Electrical Stimulation of PC-12 Adh Cells on BPLPAT Films and Scaffolds:* A homemade device was used for electrical stimulation on PC-12 Adh cells. Cells were seeded at a density of  $3 \times 10^4$  cells mL<sup>-1</sup> in cell differentiation culture media (F-12K medium supplemented with 1% horse serum, 1% antibiotics and 50 ng mL<sup>-1</sup> nerve growth factor (NGF)) on BPLP, BPLPAT5%, BPLPAT10%, and BPLPAT15% films (2 cm × 2 cm), and allowed to adhere for 24 hrs. A 100

mV mm<sup>-1</sup> potential was then applied for 2hrs, and the cells were cultured for another 24 hrs.

Films were then fixed with 2.5% glutaraldehyde for SEM. Experimental processes conducted on BPLPAT scaffolds were the same as that for BPLPAT films, but with higher cell density (1×10<sup>6</sup> cells mL<sup>-1</sup>).

*Animal Studies:* To assess foreign body inflammatory responses towards BPLPAT materials, sterilized disk-shaped BPLP, BPLPAT5%, and BPLPAT10% films (~ 6 mm in diameter, ~0.2 mm in thickness) were implanted subcutaneously in the back of 8 week old female Sprague Dawley (SD) rats (ENVIGO), with PLLA films of the same shape as control. Four films (PLLA, BPLP, BPLPAT5%, and BPLPAT10%) were implanted in the upper and lower back of each rat, and 16 SD rats were divided into four groups for four time points (1, 4, 8 and 24 weeks). At each time point, rats were sacrificed with CO<sub>2</sub>, and polymer films with surrounding tissues were harvested and embedded in cryo-matrix for cryo-section. After sectioning, hematoxylin and eosin (H&E) staining (Leica) and CD11b staining (Purified anti-rat CD11b/c primary antibody and HRP Goat anti-mouse IgG (minimal x-reactivity) second antibody, Biolegend) were performed to analyze material foreign body response. Stained slides were examined using a Nikon Eclipse Ti-U microscope (Nikon Corp., Japan). Cell numbers and CD11b+ cells numbers in a 200 × 200 μm<sup>2</sup> region tissue near the implant films were quantitatively analyzed and averaged with ImageJ.

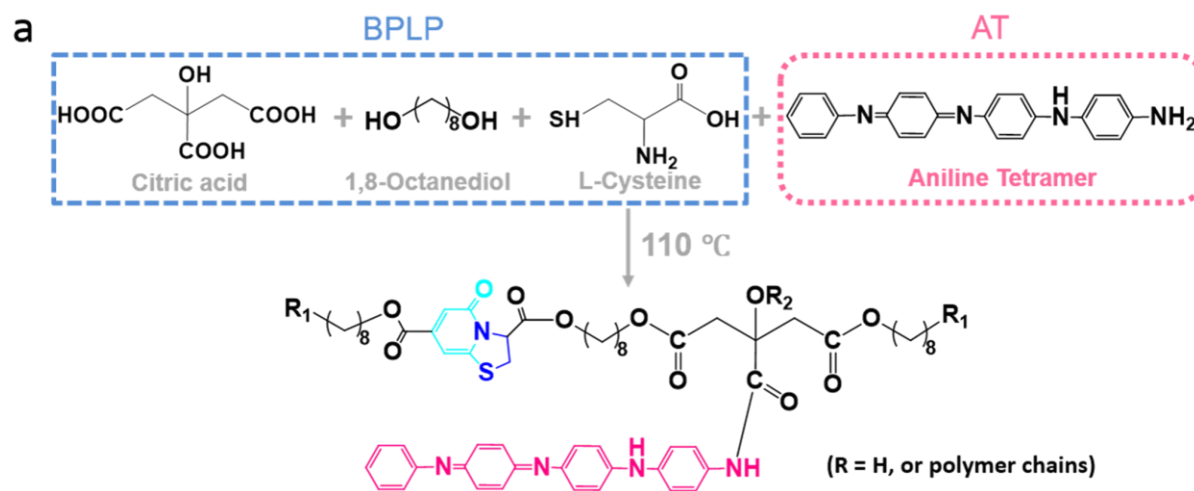


**Figure S1.** Schematic of the synthesis of BPLPAT pre-polymers.

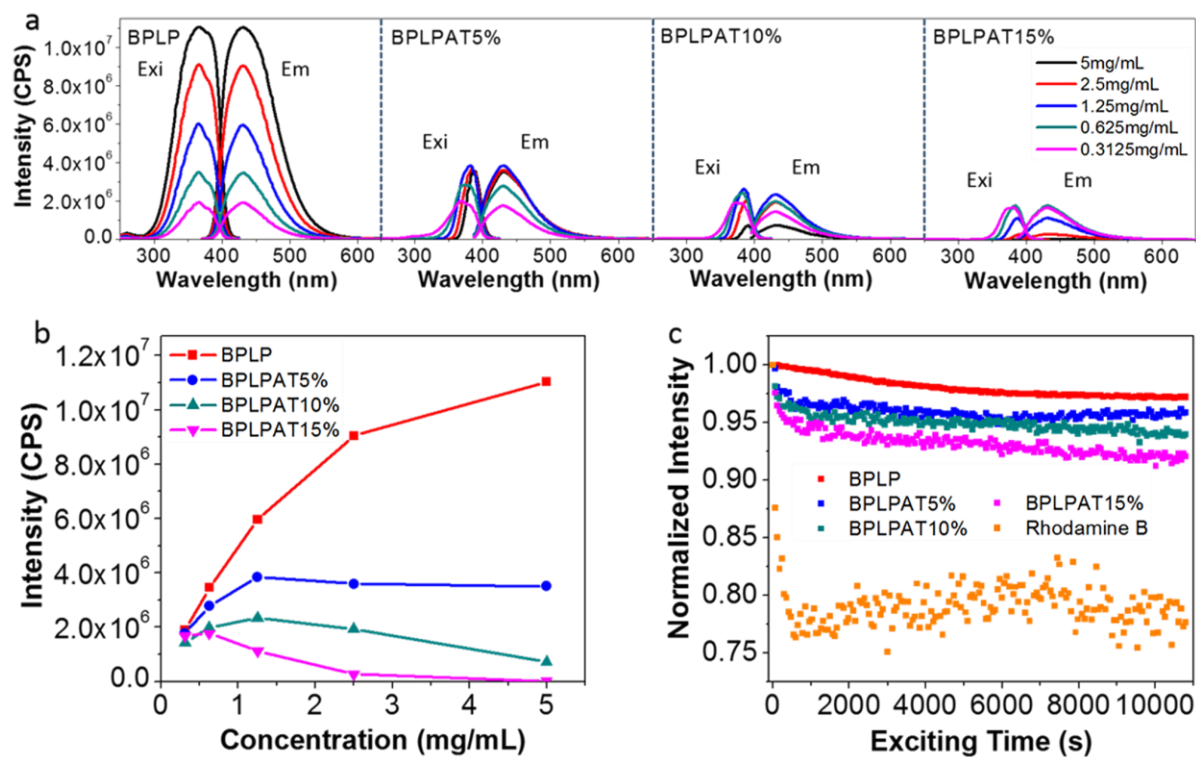


**Figure S2.** Fluorescence properties of BPLPAT pre-polymers. (a) Fluorescence intensity testing of BPLP and BPLPAT solutions at various concentrations. (b) Emission peak of BPLP and BPLPAT solutions at various concentrations. (c) Photostability of BPLP and BPLPAT solutions.

**Table 1.** Conductivity of BPLP and BPLPAT films

Samples	Conductivity (S/cm)
BPLP	N/A
BPLPAT5%	$1.06 \times 10^{-7}$
BPLPAT10%	$4.32 \times 10^{-7}$
BPLPAT15%	$2.94 \times 10^{-6}$

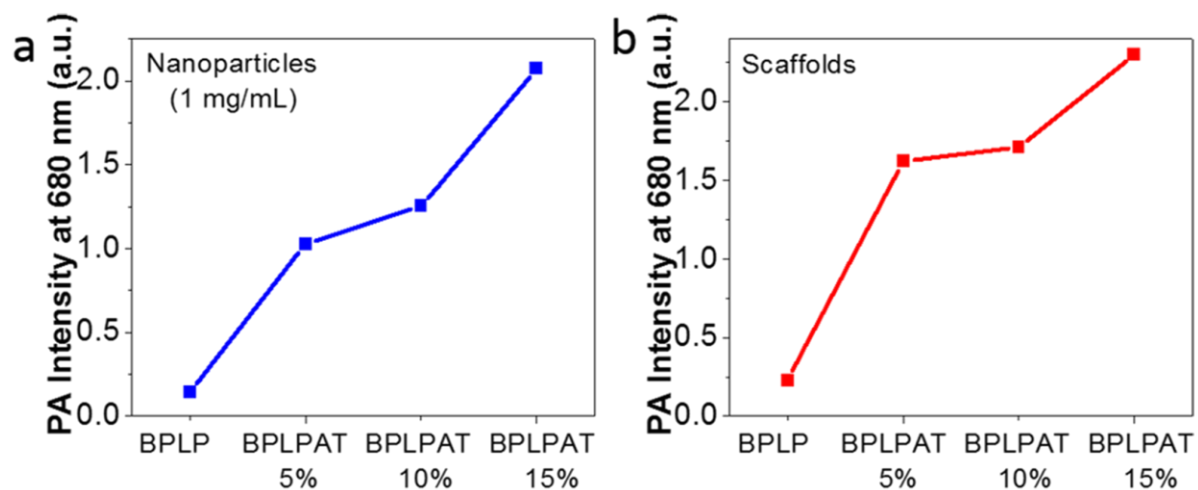


**Figure S3.** PA intensities of BPLP and BPLPAT nanoparticles and scaffolds. (a) PA intensities of BPLP and BPLPAT nanoparticle solutions (1 mg/mL) the excitation wavelength of 680 nm. (b) PA intensities of BPLP and BPLPAT scaffolds at the excitation wavelength of 680 nm.

**Table 2.** Size and Zeta potential of BPLP and BPLPAT nanoparticles.

Nanoparticles	BPLP	BPLPAT5%	BPLPAT10%	BPLPAT15%
Size (nm)	164.3 ± 6.9	178.2 ± 4.3	182.6 ± 2.0	181.9± 5.7
Zeta potential (mV)	-55.5 ± 2.0	-60.2 ± 0.6	-59.3 ± 2.8	-49.1± 0.7

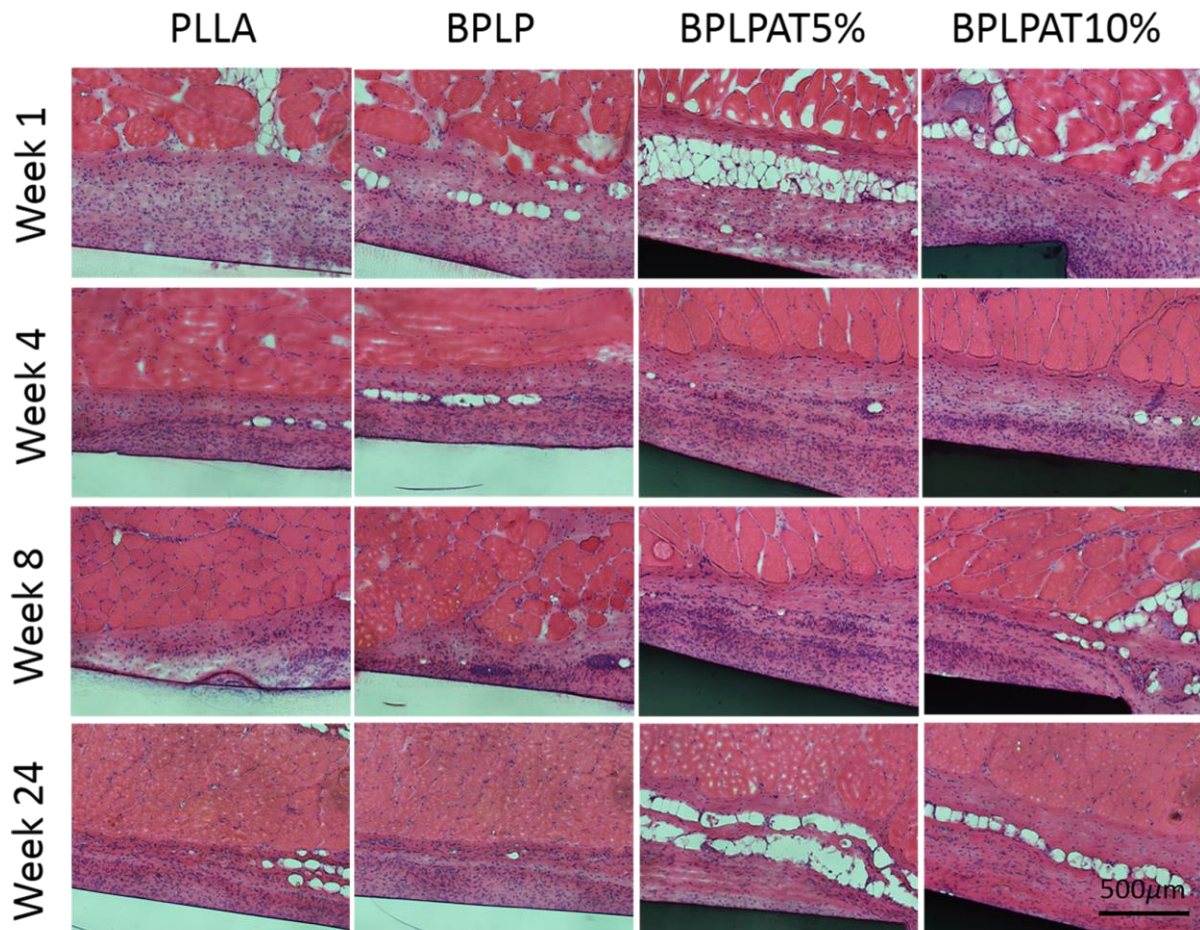


**Figure S4.** Foreign body response evaluations. Images of hematoxylin and eosin (H&E) staining of sections of subcutaneously implanted polymer films (PLLA, BPLP, BPLPAT5%, and BPLPAT10%) with surrounding tissues. Samples were harvested at 1 week, 4 weeks, 8 weeks, and 24 weeks following implantation.

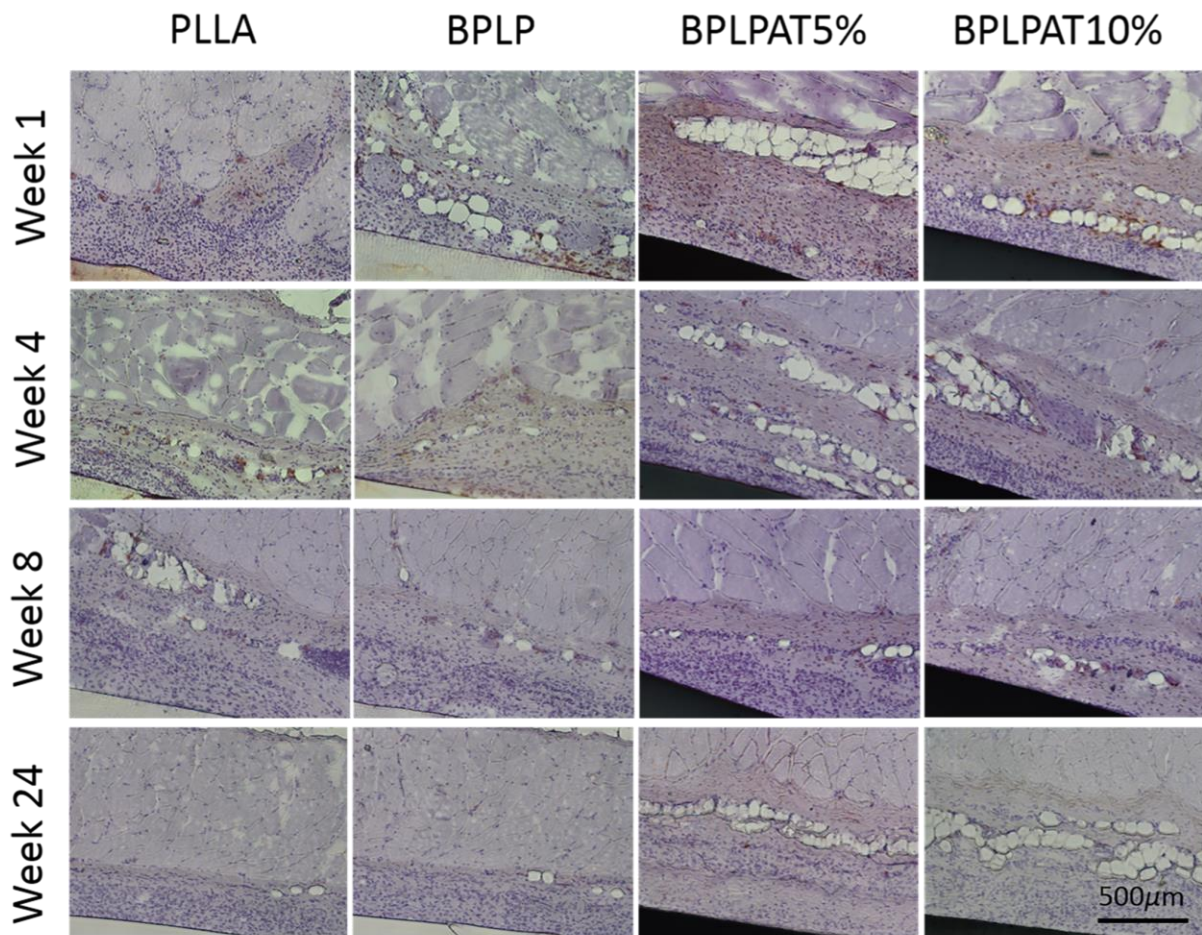


**Figure S5.** Foreign body response evaluations. Representative images of immunohistochemical (CD11b) staining of sections of subcutaneously implanted polymer films (PLLA, BPLP, BPLPAT5%, and BPLPAT10%) with surrounding tissues. Samples were harvested at 1 week, 4 weeks, 8 weeks, and 24 weeks following implantation.